AIAA JOURNAL
Vol. 47, No. 7, July 2009

Shock-Wave/Boundary-Layer Interactions in a Model Scramjet Intake

L. Krishnan[*] and N. D. Sandham[†]
University of Southampton, Southampton, England SO17 1BJ, United Kingdom
and
J. Steelant[‡]
ESA, 2200 AG Noordwijk, The Netherlands

DOI: 10.2514/1.41107

An air intake for a Mach 8 flight vehicle concept has been studied using large-eddy simulation with flow conditions corresponding to typical wind-tunnel tests. The flow contains several types of shock-wave/boundary-layer interaction for which large-eddy simulation has advantages over conventional Reynolds-averaged Navier–Stokes approaches. Laminar-to-turbulent transition was triggered using localized blowing trips in the first external ramp surface close to the intake leading edge. The trips lead to turbulent spots that propagate within an otherwise laminar flow, with a lateral spreading angle consistent with previous studies. The transitional/turbulent shock interaction near the first compression corner was found to enhance the transition to turbulence, leading to a fully turbulent boundary layer after the interaction. Further downstream, a large separation zone forms due to the cowl-lip shock wave impinging on the vehicle-side boundary layer. Perturbations from the vehicle-side turbulent boundary layer were found to enter the cowl-side boundary layer. The final transition of this boundary layer occurred at the end of a separation bubble created by the first cowl-side compression ramp. Statistics for the turbulent flow entering the combustor inlet show thick nonequilibrium turbulent boundary layers and trapped compression waves.

Nomenclature

C = model constant
E = total energy
e = internal energy
k = turbulence kinetic energy
M = Mach number
Pr = Prandtl number
p = pressure
q = heat flux
Re = Reynolds number
S = strain rate magnitude
T = timescale
t = time
u, v, w = velocity components, u_i
x, y, z = spatial coordinates, x_i
Δ = filter width
μ = viscosity
ν = kinematic viscosity
Π = pressure ratio
ρ = density
τ = shear stress

Subscripts

aw = adiabatic wall
mts = mixed time scale
s = subgrid
sep = separation
t = turbulent
w = wall
0 = reference point

Superscript

s = subgrid

I. Introduction

THE main challenge of designing intakes for high-speed airbreathing vehicles is to compress a relatively large mass flow rate with the least amount of total pressure loss, while still being robust enough to prevent unstart. Different possibilities exist, of which the Busemann intake has one of the best performances, mainly due to the fact that a large part of the compression occurs in an isentropic way. Unfortunately, this approach leads to very long intakes, which are also hard to start (Billig and Kothari [1]). A simpler approach consists of splitting the total compression into a series of oblique shock waves, each resulting in a similar pressure increase. The efficiency of an intake compression process depends strongly on the boundary layer over the intake surface (i.e., laminar, turbulent, or transitional), which can also have a significant influence on the combustor performance. The nature of the boundary layer is particularly important when small-scale experiments or flight tests are used to develop a full-scale engine, because laminar and transitional flow effects may be crucial at small scale, but negligible at the full scale. The principal aim of the present work is to investigate the flow physics in a representative intake, including compressions ramps, convex corners, impinging shock waves, and a mixture of laminar and turbulent boundary layers.

Shock-wave/boundary-layer interactions (SWBLI) (see Dolling [2] for a review) are an important phenomenon in intakes, occurring wherever there is a change in surface geometry or where shocks impinge on other surfaces. When the pressure jump across a shock is sufficiently high, the resulting adverse pressure gradient will lead to separation of the boundary layer. This is more likely when the boundary layer is laminar, but also occurs for turbulent flow. If the separated regions grow with time, it may not be possible to start the intake. Laminar interactions with large regions of separated flow may be common at the lower Reynolds numbers encountered in

---

Received 19 September 2008; revision received 10 December 2008; accepted for publication 23 December 2008.

[*] Research Fellow, School of Engineering Sciences.

[†] Professor, School of Engineering Sciences. Senior Member AIAA.

[‡] Senior Research Engineer, European Space Research and Technology Centre, Section of Aerothermodynamics, Keperlaan 1. Member AIAA.

laboratory experiments or small flight tests. Simulations of the evolution of small disturbances have been made for both ramp and shock impingement cases (Pagella et al. [3]), showing essentially the same behavior. Fully turbulent interactions (Dupont et al. [4]) are known to exhibit an additional phenomenon of large-amplitude oscillations in wall pressure over a broad band of low frequencies. Such low-frequency motions occur under the foot of reflected shock waves and are an important consideration in the structural design of an intake.

The context for the present investigation is the European project LAPCAT (Long-Term Advanced Propulsion Concepts and Technologies), which is aimed at technology development for civil application of hypersonic flight (Steelant [5]). One of the configurations is a Mach 8 vehicle operating as a scramjet in cruise condition. For intake design, one-dimensional inviscid flow analysis and Reynolds-averaged Navier–Stokes (RANS) methods are widely used. A quick indication of the potential for boundary-layer separation on the intake can be obtained from Korkegi's [6] correlations. This assessment allows the identification of locations of possible concern and indicates where design alterations are needed. The initial intake generated for the Mach 8 LAPCAT vehicle (denoted as LC01k) made use of the forebody of the vehicle, followed by two additional ramps on the vehicle side (Henckels et al. [7]). The cowl generated two further oblique shock compressions before the mass flow turned after the expansion corner into the isolator or combustor. As the initial design was driven by inviscid theory, SWBLI or any other viscous effects were not taken into account.

Experiments are needed to verify the designed intake performance. However, conducting high-speed intake experiments in a low-noise wind tunnel to match atmospheric conditions is a difficult task, particularly when transitional effects may be important. With continuing increases in computing power, three-dimensional turbulent flow simulations (large-eddy or direct numerical simulation) are becoming more common for model problems (Pirozzoli and Grasso [8], Loginov et al. [9], and Wu and Martin [10]), though, to the best of the authors' knowledge, these have not been applied to a complete intake until the present project.

The numerical approach adopted here is the method of large-eddy simulation (LES). This approach offers a more physically realistic model compared with RANS and is more cost-effective than direct numerical simulation (DNS). However, for accuracy in attached and separated boundary-layer flows, fine-grid resolutions must still be used. Depending on the data required, the overall cost of a high-resolution LES is typically 2 orders of magnitude less than a DNS. In one important sense, LES is easier for some high-speed flows. Typically, one is comparing with wind-tunnel experiments in which the wall temperature is comparable with the adiabatic wall temperature. Because viscosity increases with temperature, the local boundary-layer Reynolds numbers tend to be lower than in equivalent scale flows at low Mach numbers. An objective of the present work is therefore to study the performance of LES at hypersonic speeds and to assess its current utility for intake design and flow analysis. To perform a more realistic simulation, the approach taken in the present study is to start with a laminar flow and then trigger laminar-to-turbulent transition via turbulent spots. The simulations include multiple SWBLI, as well as an unforced transition of the cowl-side boundary layer. Throughout the paper, we will attempt to relate the complex phenomena seen in the full intake simulation to results from simpler model studies in the literature.

II. Large-Eddy Simulation Methodology

The basic equations that govern the unsteady compressible flow are the well-known Navier–Stokes equations. A dimensionless form of the equations is considered, based on reference quantities that will be given later. For application to LES, the spatially filtered equations for mass, momentum, and energy conservation may be written as

$$\frac{\partial \bar{\rho}}{\partial t} + \frac{\partial \bar{\rho}\tilde{u}_i}{\partial x_i} = 0 \tag{1}$$

$$\frac{\partial \bar{\rho}\tilde{u}_i}{\partial t} + \frac{\partial \bar{\rho}\tilde{u}_i\tilde{u}_j}{\partial x_j} = -\frac{\partial \bar{p}}{\partial x_i} + \frac{\partial \tilde{\tau}_{ij}}{\partial x_j} - \frac{\partial \tilde{\tau}^s_{ij}}{\partial x_j} \tag{2}$$

and

$$\frac{\partial \tilde{E}}{\partial t} + \frac{\partial (\tilde{E} + \bar{p})\tilde{u}_i}{\partial x_i} = -\frac{\partial \tilde{q}_i}{\partial x_i} - \frac{\partial \tilde{q}^s_i}{\partial x_i} + \frac{\partial (\tilde{u}_i\tilde{\tau}_{ij})}{\partial x_j} - \frac{\partial (\tilde{u}_i\tilde{\tau}^s_{ij})}{\partial x_j} \tag{3}$$

where an overbar denotes a filtered quantity and a tilde denotes a Favre-filtered (density-weighted) quantity. Subgrid-scale (SGS) terms to be modeled are given a superscript s. The total energy is given by

$$\tilde{E} = \bar{\rho}(\tilde{e} + \tfrac{1}{2}\tilde{u}_i\tilde{u}_i) \tag{4}$$

where e is the specific internal energy. The fluid is assumed to be perfect with the filtered pressure obtained using the equation of state:

$$\bar{p} = (\gamma - 1)\bar{\rho}\,\tilde{e} \tag{5}$$

For a Newtonian fluid, the viscous stress tensor is given by

$$\tilde{\tau}_{ij} = \frac{\mu}{\mathrm{Re}}\left(\frac{\partial \tilde{u}_i}{\partial x_j} + \frac{\partial \tilde{u}_j}{\partial x_i} - \frac{2}{3}\delta_{ij}\frac{\partial \tilde{u}_k}{\partial x_k}\right) \tag{6}$$

where μ is the viscosity and δ_{ij} is the Kronecker delta function. The heat flux is calculated using the Fourier law of heat conduction as

$$\tilde{q}_i = -\frac{\gamma\mu}{RePr}\frac{\partial \tilde{e}}{\partial x_i} \tag{7}$$

where Pr is the Prandtl number, which is set to 0.72 in the present study. The variation of the dynamic viscosity with temperature is accounted for by Sutherland's law, with a constant of 110 K and a reference temperature of 61 K.

The SGS stress tensor representing the effects of the unresolved turbulent scales is given by

$$\tilde{\tau}^s_{ij} = \overline{\rho u_i u_j} - \bar{\rho}\tilde{u}_i\tilde{u}_j \tag{8}$$

and is modeled with an eddy viscosity approach as described subsequently. The subgrid-scale heat flux is also modeled using an eddy viscosity as

$$\tilde{q}^s_i = -\frac{\gamma\mu_t}{Pr_t}\frac{\partial \tilde{e}}{\partial x_i} \tag{9}$$

where Pr_t is the turbulent Prandtl number, which is set to unity in the present simulations. Additional SGS terms due to the nonlinearity of the viscous stress and the heat flux are not modeled (see Vreman et al. [11] for a discussion of these terms).

A simple mixed-time-scale (MTS) model was preferred in the current study to the dynamic Smagorinsky model (which was also programmed) due the ability of the MTS model to capture turbulent spots. The model (Inagaki et al. [12]) is inherently local and, in contrast to the standard implementation of the dynamic Smagorinsky model, does not require averaging along a homogeneous direction. The MTS model defines the eddy viscosity as being proportional to a measure of the kinetic energy in the small scales and a model time scale: that is,

$$\mu_t = C_{\mathrm{mts}}\bar{\rho}k_sT_s \tag{10}$$

with

$$k_s = (\tilde{u}_i - \hat{\tilde{u}}_i)^2 \tag{11}$$

and

$$T_s^{-1} = \left(\frac{\Delta}{\sqrt{k_s}}\right)^{-1} + \left(\frac{C_t}{|S|}\right)^{-1} \tag{12}$$

The kinetic energy measure k_s is obtained by explicitly filtering the velocity field as denoted with the caret symbol. In this study, a top-hat filter was used to carry out this operation. The two time scales of the MTS model are $|S|^{-1}$, where $|S|$ is the strain rate magnitude, and $k_s^{-1/2}\Delta$, where the filter width is given by $\Delta = (\Delta_1 \Delta_2 \Delta_3)^{1/3}$ and the grid spacing in each direction is denoted by Δ_i. The actual time scale is defined as a harmonic average of these two time scales. Inagaki et al. [12] showed that the model does not require additional van Driest-type damping terms to cope with near-wall flows. They recommended values of 0.05 and 10 for the model parameters C_{mts} and C_t, respectively. Following tests for compressible turbulent channel flow, the constant C_{mts} was reduced from 0.05 to 0.03 and then kept fixed for all our LES studies (see also Touber and Sandham [13], in which the model was compared with dynamic Smagorinsky for a model SWBLI problem). Several compressibility corrections to the model were tested, but none gave significantly better results, so no other changes to the model were made. Compressibility corrections are believed to have little effect because the flows have generally been well resolved and the most important compressibility effects are captured in the resolved scales. If one were using coarser grids, the subgrid modeling would be more important and compressibility effects would need more attention. At higher Mach numbers than those considered here, one would also expect to have to include real-gas effects into the subgrid modeling.

The governing equations are solved using a stable high-order code with shock capturing. An entropy splitting approach is used and all the spatial discretizations are done using a fourth-order central-difference scheme, and the time integration is done using the third-order Runge-Kutta method. Stable high-order boundary schemes are used along with a Laplacian formulation of the viscous and heat conduction terms to prevent any odd–even decoupling associated with central schemes. More details of the method can be found in [14,15]. The fully parallel version of the preceding scheme has been successfully used to simulate transonic flow over bump [16], turbulent spots [17,18], and transitional SWBLI [19]. No-slip fixed-temperature boundary conditions are applied at solid surfaces, and freestream and outflow boundaries use characteristic methods to reduce reflections.

To remove the numerical grid-to-grid oscillations due to the central finite difference schemes, a sixth-order standard centered explicit filter is used (Bogey and Bailly [20]). For the present study, a sixth-order filter was used. The selective filtering is applied only in the streamwise and the spanwise directions, in which the grids are equally spaced for all the test cases considered. Selective filtering is only needed when the present code is run in LES mode. Validation and grid issues are addressed later in this paper (Sec. IV.C).

III. Intake Geometry

For the scramjet-propelled LAPCAT Mach 8 vehicle with a ventrally positioned propulsion unit, an intake was designed according to thrust and mass flow requirements established at a system design level. The design requirements were challenging, as a pressure ratio of $\Pi = 50$ needed to be achieved with as low a total pressure loss as possible. The initial design is denoted as LC01k [7]. It consists of three external compressions (a forebody and two ramps) and two internal compressions (cowl) (Fig. 1a). The related wind-tunnel model is based on this configuration but without the forebody. The freestream Mach number at which the model is tested corresponds to the one downstream of the forebody-generated oblique shock.

Because of the large overall pressure ratio, one has to be assured that the wind-tunnel intake is robust and can withstand the SWBLI without separating the boundary layer. The likelihood of boundary-layer separation is assessed at different locations along the ramp and cowl by applying the criterion of Korkegi [6],

$$M_0 < 4.5\colon \frac{p_{\mathrm{sep}}}{p_0} = 1 + 0.3M_0^2 \quad M_0 \geq 4.5\colon \frac{p_{\mathrm{sep}}}{p_0} = 0.17M_0^{2.5} \qquad (13)$$

according to which separation could occur at the position x, where $p_x > p_{\mathrm{sep}}$. The subscript 0 refers to the conditions at the origin of the boundary layer. For configurations with bleed, an indication of separation on the ramps aft of the bleed is done by taking the first segment after the bleed as a reference. The Korkegi criterion has been used successfully within scramjet combustors, and it is of interest here to explore its relevance to hypersonic intakes. Configurations highlighted as possibly critical according to this criterion were examined in more detail by computational fluid dynamics (CFD) and, in some cases, also experimentally.

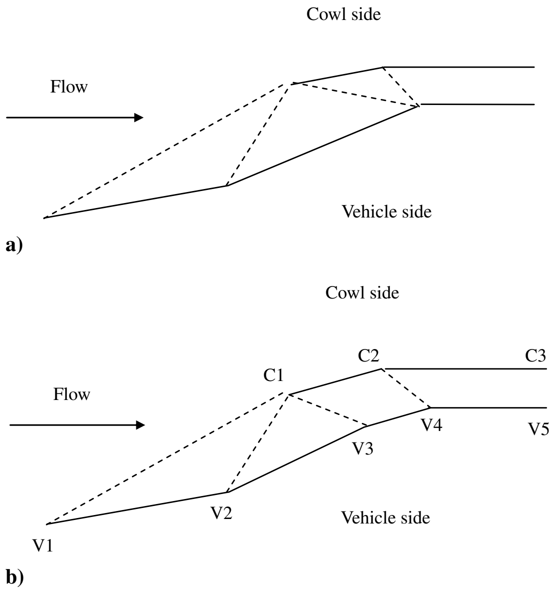

Fig. 1 Schematic of the inviscid flowfield for a) the LC01k intake and b) the modified LC01kx intake (not to scale).

According to Eq. (13), separation is predicted to occur for the wind-tunnel model on the vehicle side by the shocks emanating from the cowl. CFD based on a steady RANS approach (with the Spalart–Allmaras turbulence model) confirmed this. Incorporating a bleed after the second ramp meant that a separation bubble could be avoided, but at the cost of a 30% loss in precompressed mass flow and in thrust generation, which is detrimental for the overall vehicle performance. To get the full amount of thrust, the highest possible fraction of air compressed by the intake should enter the combustion chamber. To check the possibility of removing the bleed, configurations without a major modification to the design philosophy are of great interest. One promising alternative is to avoid coalescence of two impinging shocks onto the same geometrical location, hence relaxing the effect of an adverse pressure gradient on the rather thick boundary layer. The easiest way of achieving noncoalescence is to separate the shock impingement points geometrically from each other. The modified intake LC01kx, which is derived from the original one by inserting additional parts that are aligned with the cowl ramp, is shown in Fig. 1b. In this design, the pressure rise associated with the shocks emanating from C1 and C2 impinge separately on the vehicle-side boundary layer, and in each case, the inviscid design has the shock impinging at a convex corner, in an attempt to reduce the strength of the shock-wave/boundary-layer interactions. The intake has not been optimized for viscous effects and the final simulations are probably more representative of an intake operating in a slightly offdesign condition. Table 1 gives the coordinates of the points shown on the sketch. The first ramp angle is 6.5 deg and the incremental second ramp angle is 7.7 deg. The freestream Mach number at the inflow to the calculation ($x = 0$) is $M_0 = 6.0$.

Referring to Fig. 1b, the main physical processes associated with such an intake at the Reynolds numbers of wind-tunnel experiments and small flight tests are as follows:

1) Laminar-to-turbulent transition occurs along the leading edge ramp surface (from point V1 to V2).

2) A compression ramp shock wave interacts with a transitional/turbulent boundary layer (at points V2 and C2).

3) A shock-wave interacts with a turbulent boundary layer near a convex corner (at points V3 and V4).

Table 1 Geometry of the intake used for the simulations

Point	x	y	Flow angle, deg
V1	0.0	0.0	——
V2	227.7	26.0	6.5
V3	483.0	90.6	14.2
V4	517.4	93.2	4.3
V5	551.4	93.2	0.0
C1	401.1	99.8	——
C2	484.7	106.0	4.3
C3	551.4	106.0	0.0

4) Shock reflections interact with turbulent boundary layers in the isolator duct (downstream of point V4).

Both the front ramp (V1–V2) and the cowl first surface (C1–C2) are assumed to begin with laminar boundary layers. Transition is tripped along the front ramp using an injection method. No attempt is made to trip the cowl-side boundary layer.

For the present simulation, the inflow is taken 2 mm downstream of the actual leading edge. The second ramp starts at $L_x =$ 227.7 mm. The leading-edge shock was introduced at the inflow boundary by prescribing the laminar flow profiles obtained from the DLR TAU code.[§] This approach was used to save the computational cost of resolving the entropy layer near the sharp leading edge. Grid details, with a total of 9.6 million grid points, are as follows for case LC01kx: $L_x = 551.4$ mm, $L_y = 106.0$ mm, $L_z = 30$ mm, $N_x = 999$, $N_y = 161$, and $N_z = 60$.

The flow domain is discretized using equally spaced grids along the streamwise and spanwise directions and a stretched grid in the wall-normal direction, so that there are enough points near the two walls. The upper boundary of the domain uses a far-field characteristic condition up to the cowl lip, where it is replaced with a no-slip, fixed-temperature condition. All lengths are normalized using a reference length of 1 mm. Velocity, density, and temperature are normalized with the Mach 6 freestream properties and pressure with density times velocity squared for the Mach 6 inflow condition. The flow is assumed to be periodic in the spanwise direction, and no-slip fixed-temperature conditions are applied at the flat-plate surface, with $T_w = T_{aw}$ and the adiabatic wall temperature taken from the $M = 6$ inflow condition. The Reynolds number for the calculation is specified as $Re = 8399$, giving a Reynolds number based on intake length of 4.6×10^6.

An initial two-dimensional laminar simulation was carried out to obtain a starting condition for the subsequent three-dimensional LES. A laminar SWBLI resulted in a large separation bubble in the flow. Figure 2 shows an enlarged view of the density field from this simulation, starting from near the x location of the cowl leading edge. The cowl shock impinges close to the first convex corner and causes a large separation bubble that extends far upstream. For the previous (LC01k) intake design, in which both the cowl leading-edge shock and the cowl-ramp shock impinged at the same streamwise location, the pressure rise was higher and the resulting separation bubble grew indefinitely, eventually leading to a failure of the simulation, whereas the present design (LC01kx), with a weaker pressure jump, converged to a steady solution.

To start the three-dimensional LES, the two-dimensional solution was extruded in the third direction and large-amplitude disturbances were added using a localized blowing trip. This amplitude is high enough to bypass the slower linear stages of the transition process. The final breakdown of these large-amplitude disturbances occurs via the formation of localized islands of turbulence (i.e., turbulent spots). The growth and merging of these turbulent spots will result in a fully developed turbulent flow further downstream. The effects of compressibility on the spot growth also modify the transition scenario in a high-speed compressible flow, because the spot growth rate is substantially reduced by the effects of compressibility (see, for example, the experimental data collated by Fisher [21] and the DNS of Krishnan and Sandham [17]). In the present work, localized injection of fluid with a wall-normal velocity equal to 20% of the freestream velocity was used. The trip was located at $30 < x < 34$ and $13 < z < 17$ (i.e., just downstream of the inflow boundary and in the center of the domain). A train of turbulent spots was triggered with a time length of 6 nondimensional time units (based on 1 mm as reference length and the velocity of the $M = 6$ reference flow) and a time delay of 70 between successive injections (spot frequency 0.0143). The LES was run up to a dimensionless time of 2220 (i.e., about 31 spots were triggered). The total simulation time corresponded to approximately four throughflow times for the complete domain (for fluid traveling at the local freestream velocity).

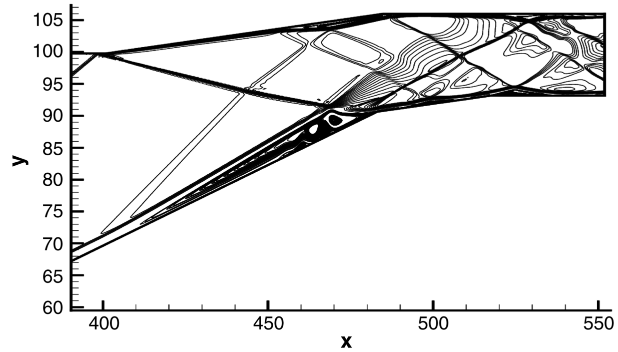

Fig. 2 LC01kx 2-D laminar flowfield (enlarged view).

IV. Results

A. Overview of the Flow Solution

An overview of the simulation results is first presented using pseudoschlieren (absolute value of the density gradient) images. Figure 3 shows pseudoschlieren images at the spanwise location $z = L_z/2$ (i.e., halfway across the domain). Figure 3a is for the whole computational domain, and Fig. 3b focuses attention on the region downstream of the cowl lip. The figures are in the correct aspect ratio to provide a better appreciation of the flow scales. Because the spots were triggered on the midplane, this figure shows the individual spots growing along the front ramp. The enhanced lateral growth rate of the spots near the compression corner at $x = 225$ means that the flow after this point is effectively turbulent across the whole span. Working downstream from the front of the domain, we can identify the shock waves as the first ramp shock (starting at $x = 0$), the second ramp shock (starting at $x = 225$), and the cowl-lip shock (starting from the cowl lip at $x = 401$). The cowl-lip shock, although designed (using inviscid methods) to hit the convex corner at $x = 483$, in fact causes a separation of the boundary layer ahead of the corner. A reflected shock, originating from the boundary-layer separation point, is the next shock wave seen in the flow. This shock wave impinges on the cowl surface near $x = 495$, where it undergoes a regular reflection. Although less clear, a further shock wave seems to form from near the convex corner, due to the streamline curvature near the reattachment point. This shock wave impinges on the cowl surface near $x = 507$ and also reflects, although by now as a weaker compression wave. More details of the flow in the later parts of the intake will be discussed after we have considered the transition processes in more detail.

B. Transition Mechanisms and Flow Structures

Transition on the vehicle surface takes place via the growth of turbulent spots. This is illustrated in Fig. 4 by means of plots of surfaces of the second invariant of the velocity gradient tensor. Figure 4a shows a plan view of the first ramp and part of the second ramp, illustrating the growth of turbulent spots and the eventual formation of a fully turbulent boundary layer. Figure 4b shows a close-up of the structure of one of the developing turbulent spots, which can be seen to be composed of an array of hairpinlike structures. The present spots are comparable in form with the "young" turbulent spots described by Singer [22], however, the growth rates

---

[§] Private communication with S. Karl, 2007.

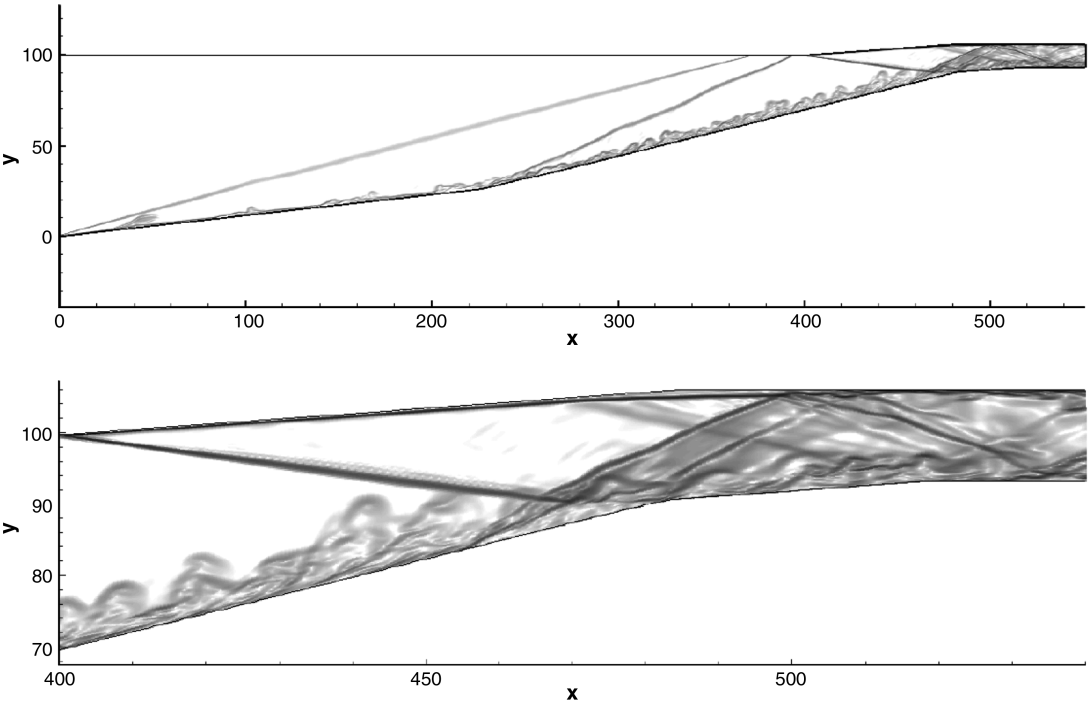

Fig. 3 **Pseudoschlieren (magnitude of density gradient) at $z = L_z/2$: whole domain (top) and close-up view from the cowl lip onward (bottom).**

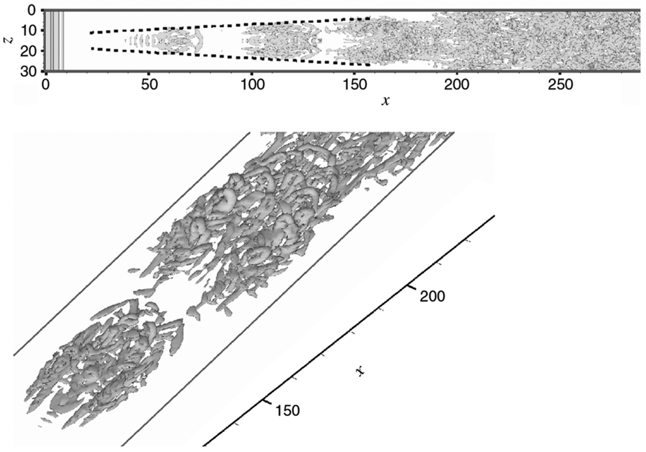

Fig. 4 **Surface of second invariant, showing a) plan view and b) close-up of turbulent spots developing on the first ramp surface.**

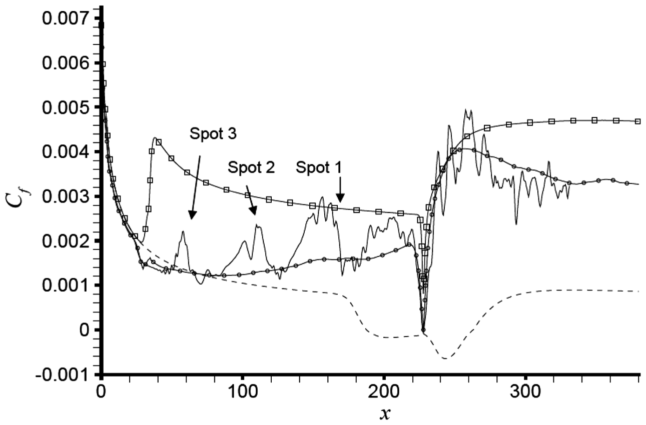

Fig. 5 **Skin-friction variation through the first ramp interaction: RANS/Spalart–Allmaras (squares), laminar (dashed), averaged LES (circles), and instantaneous LES result averaged over a spot width (solid line).**

here are significantly reduced. The growth rate is around one-third of the growth rate of a turbulent spot in incompressible flow. A lateral half-spreading angle of 3.4 deg was measured from the present simulations, putting it between the Mach 4 and Mach 6 cases from [17]. Explanations for the reduction of growth rate have focused on the role of instability mechanisms in the spot wingtip region and the stabilizing effect of compressibility [17]. Figure 5 shows the surface skin friction c_f obtained by averaging over either an appropriate spot width ($10 < z < 20$) (solid line) at a fixed time or over the entire span and over time (circles). The figure also shows the steady RANS (Spalart–Allmaras model) c_f predictions from the DLR TAU code (squares) and the laminar c_f distribution (dashed line). The laminar solution leads to a large separation zone starting from $x = 180$, whereas the transitional case does not have any separated flow in the mean. The span-averaged c_f includes the laminar region surrounding the isolated spot, and so c_f is significantly lower than the local turbulent values inside the spots. Within the turbulent spots, c_f increases to the fully developed turbulent value. The RANS solution (with the turbulence model activated from the inflow) gives a rapid transition to turbulence and also leads to higher values of c_f after the interaction. This is in contrast to the LES, which shows a local maximum of c_f just after the interaction.

In the present case, the flow appears to be composed of distinct turbulent spots before the ramp interaction, but is essentially fully turbulent after it (because the averages over the central region are comparable with the full-span averages). The situation is reminiscent of the case of turbulent spots propagating through a zone of separated flow created by impinging a shock wave on a boundary layer (Krishnan and Sandham [18]). In that case, it was observed that the turbulent spot lateral growth rate increased by as much as a factor of 3 during the interaction with an originally laminar separation bubble. At the same time, the flow under the spot locally reattaches as the spot crosses the bubble. The increased lateral spreading angle was attributed to the increased strength of the lateral shear layer that drove the wingtip instability and hence spot growth rate. The same physical process appears to be happening in the present ramp interaction at higher Mach numbers, leading to a fully turbulent flow after the ramp interaction. For RANS calculations, the first compression corner may thus be a better location to force transition than the start of the calculation.

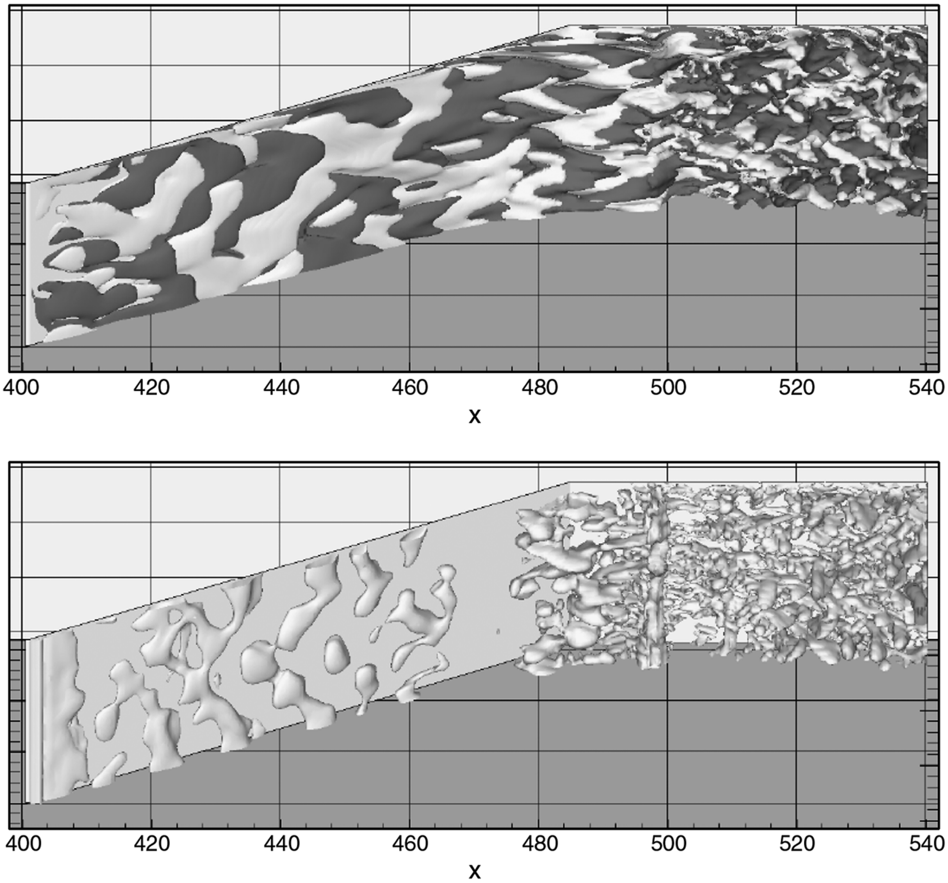

Fig. 6 View looking up at the cowl inner surface: streamwise vorticity (top) and second invariant (bottom).

The transition scenario in the cowl boundary layer is illustrated in Fig. 6 by means of vorticity and second invariant contours. Here, we are looking upward at the internal cowl surface and the vehicle surface has been removed for clarity. The influence of perturbations from the vehicle-side turbulent boundary layer can be seen upstream of the cowl corner. These structures are relatively low in amplitude inside the boundary layer and are caused by disturbances propagating (in the form of sound waves) from the turbulent boundary layer on the second ramp. A receptivity process leads to these waves getting inside the boundary layer, from which position they can grow and influence the boundary-layer transition process. In this case, the transition is not immediate and occurs after the boundary-layer separation caused by the compression ramp on the cowl. Downstream of the cowl corner, the separated shear layer is found to reattach as a turbulent boundary layer. Hairpin-shaped coherent structures are identified in the downstream turbulent boundary layer. The spanwise coherent structures near the reattachment location are due to the impinging shocks from the vehicle side.

Although disturbances are clearly entering the boundary layer upstream of the cowl compression corner, the final transition is reminiscent of the self-sustained transition process previously observed in LES by Teramoto [23]. In that study, a laminar separation bubble generated by shock impingement onto a Mach 2 boundary layer was found to undergo a transition process at the rear of the bubble that was independent of upstream disturbances. The process only occurs at high values of the pressure rise over the bubble. We have repeated the Teramoto case with our code and found the same results; with zero upstream disturbances, the flow underwent a self-sustained transition to turbulence. The bubble was insensitive to small upstream (less than 1% amplitude), but reduced in length as the disturbance amplitude was further increased. The origins of the self-sustained motion were studied by Yao et al. [19], who identified an absolute instability in the steady vortex patterns at the rear of the bubble. This process arises at high values of pressure rise over the bubble, whereas for weaker interactions, the transition proceeded according to a convective (oblique-mode) growth of instability waves.

C. Mean Flow and Turbulence Statistics

The mean flowfield and resolved turbulence statistics are obtained by time- and span-averaging of the flow properties. The mean flowfield of the LC01kx intake is visualized by pseudoschlieren in Fig. 7a and by means of wall-normal velocity in Fig. 7b. The small separated region due to the impingement of the cowl-lip shock upstream of the first expansion corner along the vehicle side is visible. It is also clear that the expansion of the flow downstream of the shock impingement has a weakening effect on the reattachment shock. The detailed flow pattern will be sensitive to the exact location of the cowl shock impingement and this is qualitatively similar to the experimental study of Lanson and Stollery [24], who reported that intake performance was strongly affected by cowl-lip location. The separation and reattachment shocks from the vehicle-side separation bubble impinge near the reattachment location of the cowl-corner separation bubble. This makes the flowfield complicated, because we also expect a reattachment shock from the cowl-corner separation bubble. A weak shock wave from the cowl-side laminar separation location is found to impinge near the second convex corner along the vehicle side. The separated regions present within the vehicle-side and the cowl-side boundary layers are clearly visualized by the stream traces that have been added to Fig. 7b (the black lines near the surfaces).

Figure 7c shows the streamline that intersects the cowl lip and hence defines the captured stream tube of the intake. This indicates that about 90% of the flow projected onto the frontal area of the intake is actually being captured, and the remaining spillage occurs upstream of the cowl leading edge, across the intake leading-edge shock and the external compression corner shock. The mean sonic line (also shown in Fig. 7c) shows the thickening of the vehicle-side boundary layer near the first convex corner due to the strong SWBLI.

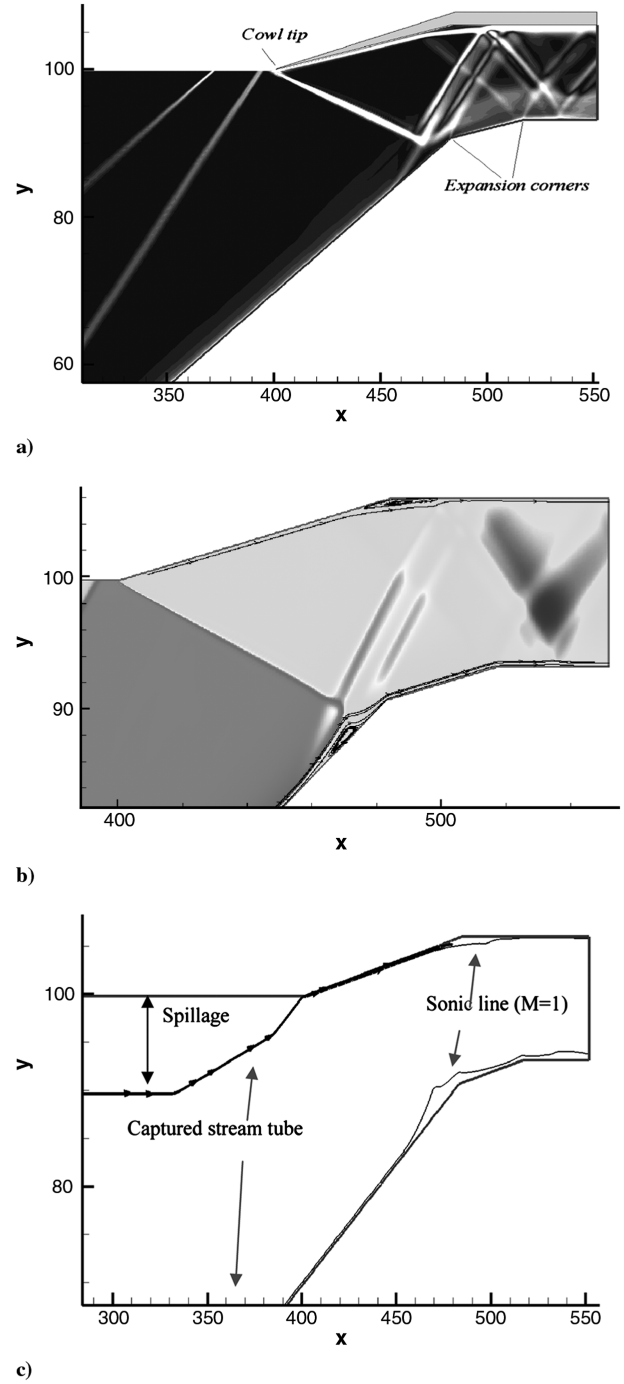

Fig. 7 LC01kx time-and span-averaged flowfields: a) LC01kx mean turbulent flowfield (pseudoschlieren enlarged view), b) wall-normal velocity distribution along with stream traces showing the separated regions due to SWBLI (not to scale), and c) the captured stream tube and the sonic line evolution along the intake (enlarged view).

This thickened subsonic region facilitates a stronger feedback of the convex corner effect in the upstream direction and counteracts the adverse pressure gradient due to the SWBLI. This plays a role in reducing the extent of the separated region and hence is acting as a separation stabilization device.

Figure 8 shows the mean skin-friction evolution along the vehicle and cowl surfaces. In the vehicle-side boundary layer (top figure), an incipient separation is seen near the external ramp corner ($x = 228$). A separated region about 30 mm in length ($450 < x < 480$) is seen upstream of the first expansion corner, caused by the cowl leading-edge shock impingement. Another small separated region is seen due to the reflected shocks in the isolator region downstream of the second expansion corner. No massive flow separations are observed for the present intake, in contrast to earlier simulations of the LC01k design. It clearly shows that the design modification (LC01kx) could cope with the adverse pressure gradient and avoid massive separation and unstart. Although Korkegi's criterion predicts separation, it fails to indicate whether the separation is contained or not. A possible reason is related to the convex geometry near the end of the intake. The sharp corner fixes the separation point of the cowl-shock-induced bubble and hence prevents it from growing or moving. A separation induced by the second shock is predicted and simulated, but remains small and locks in to the last corner.

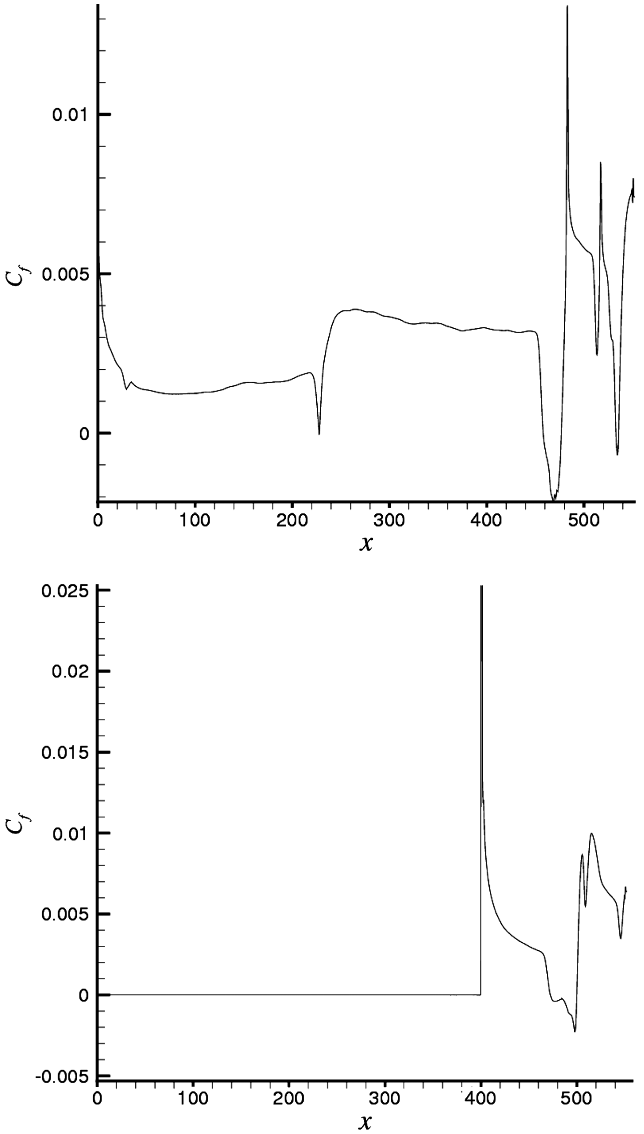

Fig. 8 Mean surface skin-friction distribution along the intake: vehicle side (top) and cowl side (bottom).

The skin-friction evolution along the cowl surface (Fig. 8b) illustrates the development of a laminar boundary layer downstream of the cowl leading edge. This confirms the turbulent reattachment of the cowl-corner separation bubble, similar to the shock-induced separation-bubble-transition case of Teramoto [23]. The capture of the transitional bubble here demonstrates the improved prediction capability offered by LES for these flows. A RANS calculation would typically have to prescribe the transition point and one would then need to check the sensitivity of the final results to this choice. LES, on the other hand, resolves the receptivity and transition mechanisms on the computational grid. It is important to note, however, that the presence of a separation is predicted by Korkegi's correlation.

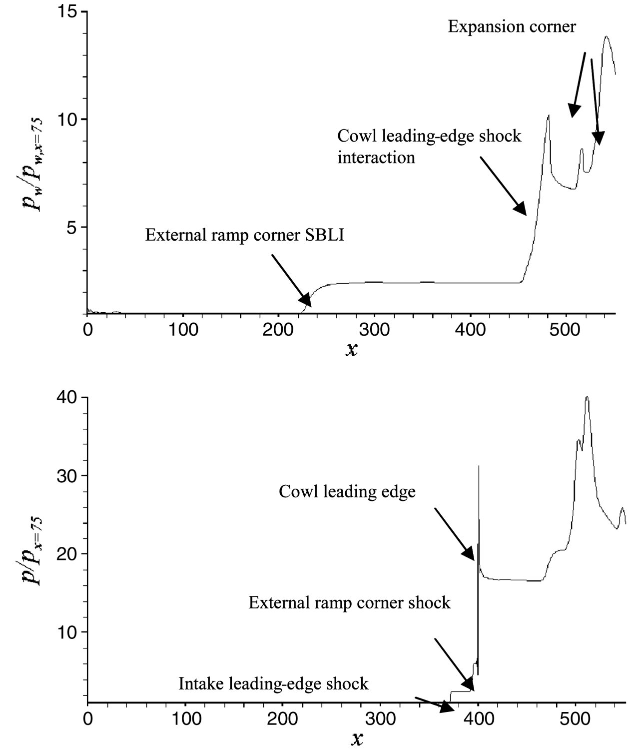

Fig. 9 Mean static pressure evolution: vehicle side (top) and cowl side (bottom).

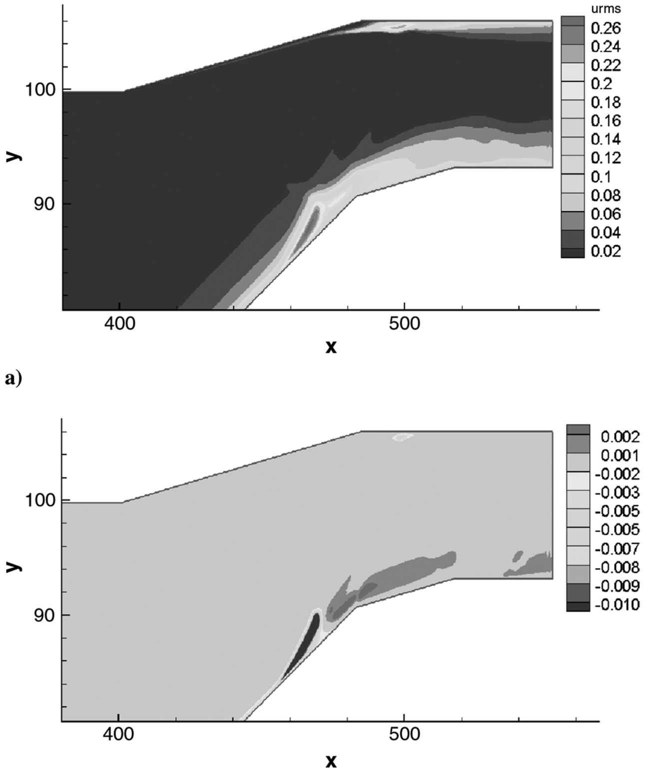

a)

b)

Fig. 11 Turbulence statistics: a) rms velocity fluctuations and b) Reynolds stress ($-u'v'$).

The mean static pressure distributions along the vehicle and the cowl surfaces are shown in Fig. 9. To aid interpretation, the pressure has been divided by the wall pressure at $x = 75$. There is a small pressure jump near the first vehicle-side compression corner at $x = 228$. Along the vehicle side, the maximum pressure jump is seen near the cowl leading-edge shock impingement around $x = 470$ (Fig. 9a). Flow expansion downstream of the convex corners is also evident. The pressure distribution along the cowl side upstream of the cowl lip (Fig. 9b) shows pressure jumps due to the intake leading-edge shock and the external ramp corner shock. There is a large

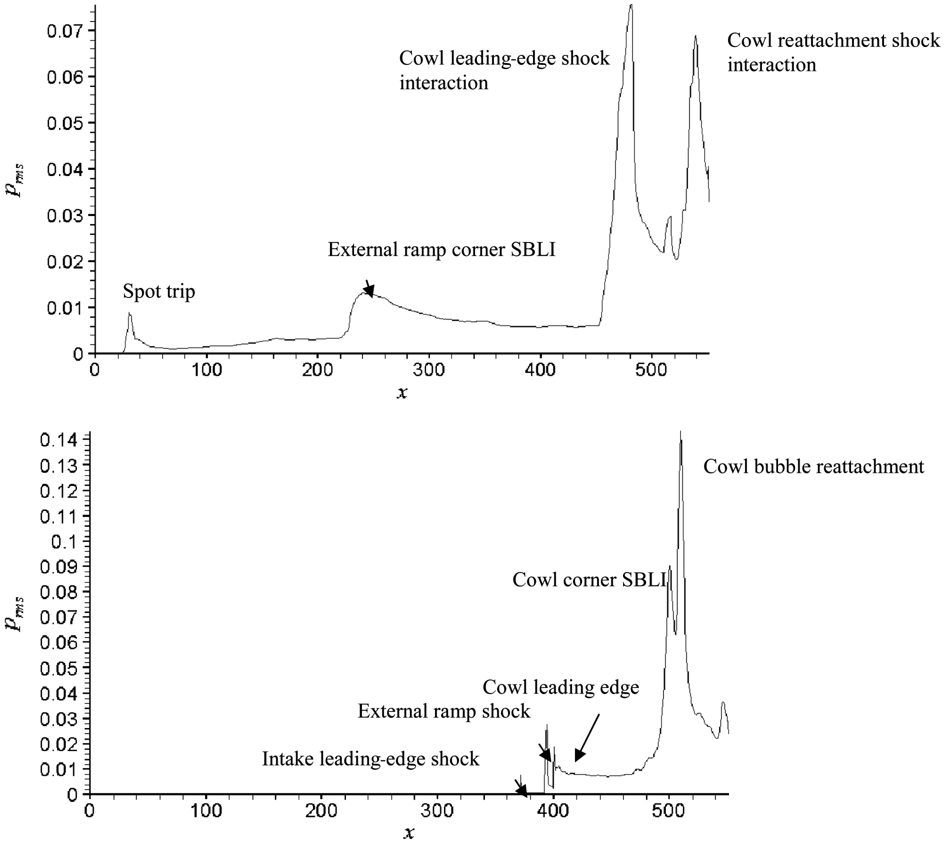

Fig. 10 Fluctuations in rms wall pressure: vehicle side (top) and cowl side (bottom).

pressure rise at the cowl leading edge and at the cowl-corner separation-bubble reattachment location.

Root-mean-square values of wall pressure fluctuations are shown in Fig. 10. These types of data are necessary for aeromechanical analysis of an intake (material fatigue analysis) and are more reliably obtained from LES than from unsteady RANS. For a corresponding flight condition (where $\rho V^2 = 128.4$ kPa at the start of the intake), the pressure fluctuations at the location at which the cowl shock meets the vehicle would be around 9 kPa. The pressure fluctuations associated with this interaction are much higher than the vehicle-side external corner ramp SWBLI. The cowl-reattachment/shock interaction shows similar levels of unsteadiness. The pressure fluctuations are smallest near the convex corners ($470 < x < 530$). The maximum unsteady pressure fluctuations along the cowl are observed near the location of cowl separation-bubble reattachment. The intensity is about double that of the cowl-corner SWBLI, due to the coincidence of the reflected cowl-lip shock and the cowl separation-bubble transition and reattachment. In the full-scale flight condition, this interaction would probably be weaker because one would expect transition to occur further upstream and hence one would not have such a large separated-flow region.

Root-mean-square velocity fluctuations are shown in Fig. 11a, using the Cartesian velocity component in the x direction. Maximum values of the velocity fluctuations are observed where the cowl-lip shock impinges on the vehicle side and near the cowl separation-bubble reattachment location. A similar structure is seen in the Reynolds stress plotted in Fig. 11b. The maximum Reynolds stress occurs upstream of the shock impingement location around $x = 470$, which is clearly an important region for turbulence production. Because the remaining distance to the end of the computational domain is only around 10 boundary-layer thicknesses, there is no space for the boundary layer to recover fully to equilibrium after this strong disturbance. Thus, a highly nonequilibrium flow will enter the combustor, along with the reflected pressure waves seen, for example, in Fig. 7a.

The present calculations were performed on a grid with approximately 9.6 million grid points. Compared with previous studies of turbulent spots, the flow upstream of the first compression corner is believed to be well resolved (grid within a factor of 2 in each direction of that required for a direct numerical simulation). For the attached boundary-layer flow after the first interaction, the grid is comparable with previous LES. For example, $\Delta x^+ = 40.7$,

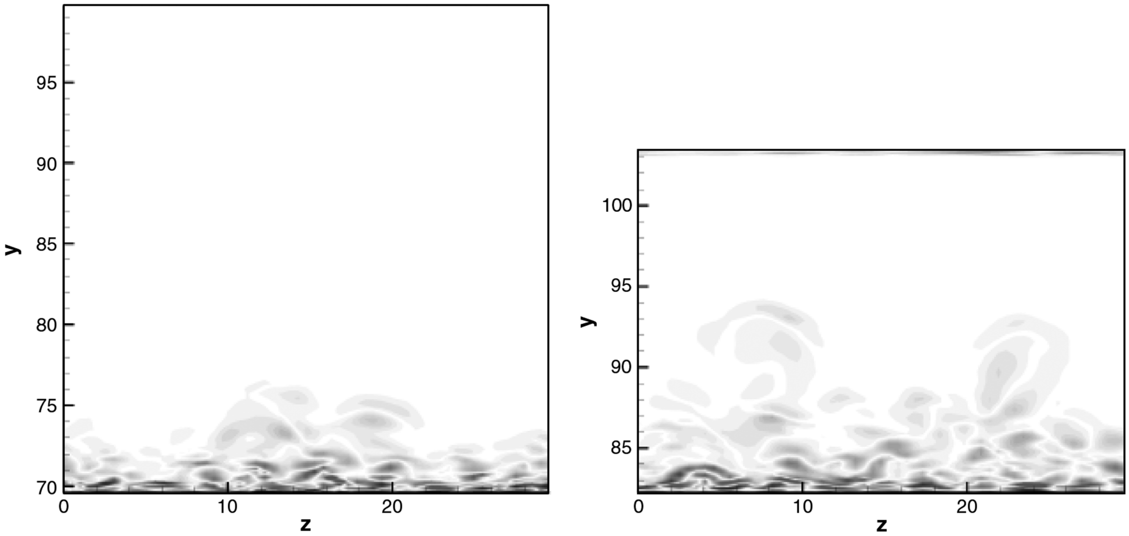

a) $x = 400$

b) $x = 450$

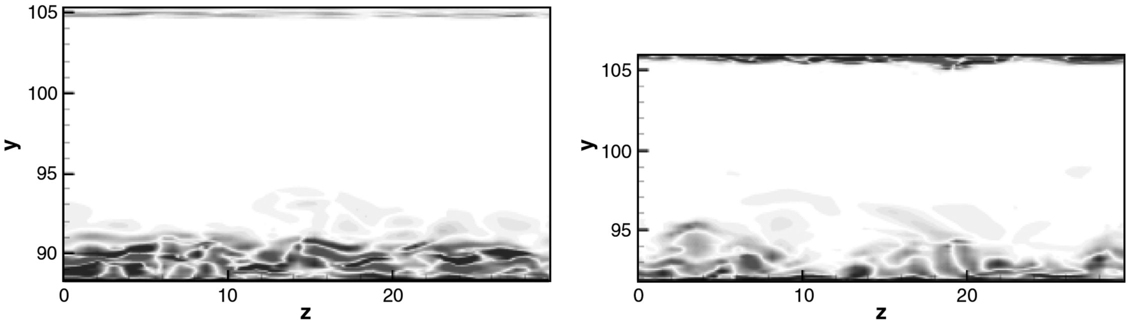

c) $x = 475$

d) $x = 500$

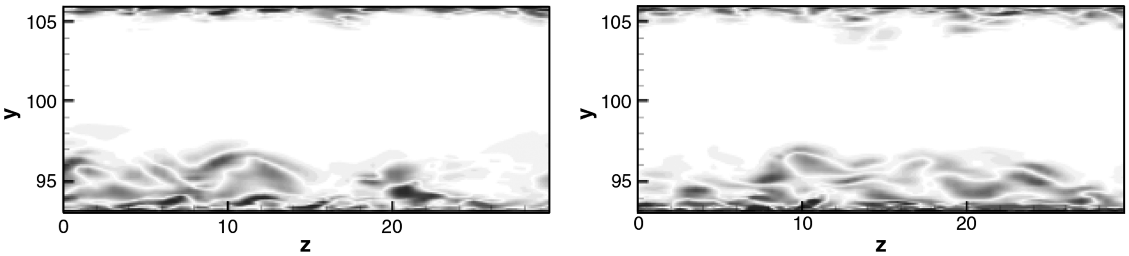

e) $x = 525$

f) $x = 540$

Fig. 12 Isocontours of streamwise vorticity over the range from −0.5 to +0.5, plotted in y–z planes at the given x locations.

compared with 54.5 from Stolz [25] and 70.2 from Teramoto [23]. In the spanwise direction, the comparable numbers are 38.3 from our simulation compared with 30.1 from Stolz [25] and 28.1 from Teramoto [23]. In the wall-normal direction, our first grid point is at $y^+ = 3.1$, compared with 4.8 from Stolz [25] and 0.74 from Teramoto [23]. In this part of the flow, the spanwise domain size in the present work is 2260 wall units, compared with 933 from Stolz [25] and 950 from Teramoto [23]. For a shock impingement model problem, a comprehensive grid resolution study was carried out by Touber and Sandham [13]. In that study, a comparable number of grid points as in the present LES were devoted to a study of the interaction between a turbulent boundary layer and a shock wave at Mach 2.3. It was found that varying the number of grid points in each direction separately had little effect on the solution. Instead, the largest effect came from the spanwise domain size. In the present study, the spanwise domain size is about 50% larger than the separation-bubble length on the vehicle side, which is significantly larger than the spanwise domain size used by Garnier and Sagaut [26] in their study of shock-induced separation. The main recommendations for future simulations would be to use a finer grid in the spanwise direction and possibly an even wider spanwise domain. The current grid and domain sizes are representative of current LES usage and are therefore appropriate for the present exploratory study.

D. Flow Properties at the Isolator Exit and Overall Intake Performance

An impression of the evolution of the flow near the end of the computational domain can be obtained from Fig. 12, which shows y–z slices through the streamwise vorticity field at various x locations given in the figure caption, extending from $x = 400$ (near the cowl leading edge) up to $x = 540$, near the end of the computational domain and the start of the combustion chamber. In this series of figures, the relatively thicker boundary layer on the vehicle side compared with the cowl side is clear. The vehicle-side boundary layer has the strongest vortical structures at $x = 475$, which is located just after the separation induced by the cowl shock. The cowl-side boundary layer is clearly turbulent from the internal compression ramp onward.

Table 2 shows averaged properties of the flow at the isolator exit. These are shown in both mass-weighted and area-averaged forms and will be used shortly to extract some measures of intake performance. As well as the averaged flow, it is also of interest to consider the distribution of flow properties across the flow. Figure 13 shows the mean density, pressure, Mach number, and temperature distribution across the end of the computational domain, which may be taken to be the inflow conditions for a subsequent simulation of the combustion chamber. The figure shows a thick turbulent boundary layer along the vehicle side (with the boundary-layer visual thickness around 5 mm). The Mach number of the core flow entering the combustor is near three. The boundary-layer thickness along the cowl side is about 2.5 mm. The wall temperature remains fixed at the adiabatic wall temperature corresponding to the $M = 6$ reference flow. The core temperature has increased from unity at the inflow to a minimum of 2.8. The maximum stagnation pressure is 23, compared with an inflow value of 31.3, whereas the maximum density is around 10 times the inflow value.

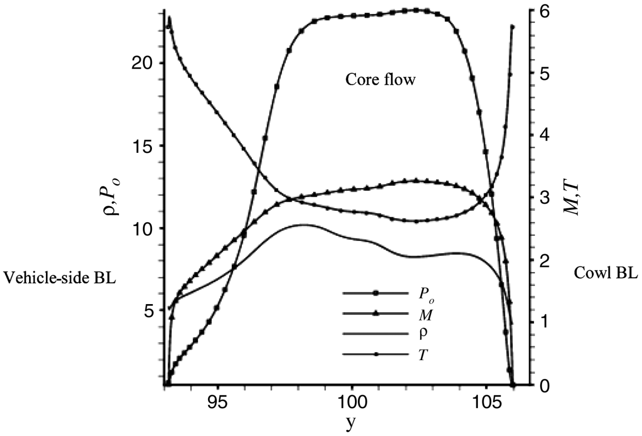

Fig. 13 Mean flow properties across the isolator exit (BL denotes boundary layer).

The mass-averaged properties at the isolator exit, given in Table 2, can be used to provide a summary of the overall performance of the intake. The ratio of the Mach number at exit to inlet is 0.483, and the total pressure ratio (the ratio of the exit total pressure to the total pressure of the $M = 6$ stream) is 0.578. The computed kinetic energy efficiency (the ratio of the square of the average velocity at the exit to the inlet) is 0.9721, which is very close to the empirical value of 0.972 (see, for example, Smart [27]). The mass capture ratio, derived from the mean flow streamlines, is 0.899. The geometric contraction ratio of the intake (the freestream capture area divided by the exit area) is 7.78, whereas the effective contraction ratio (the area under the captured streamline divided by the exit area) is 7.00. The internal

Table 2 Flow properties at the isolator exit

Property	Mass-averaged	Area-averaged
Pressure	0.517	0.565
Temperature	3.109	3.729
Total pressure	18.079	16.490
Mach number	2.895	2.767
Total temperature	8.163	8.543
Turbulence kinetic energy	0.00123	0.00137

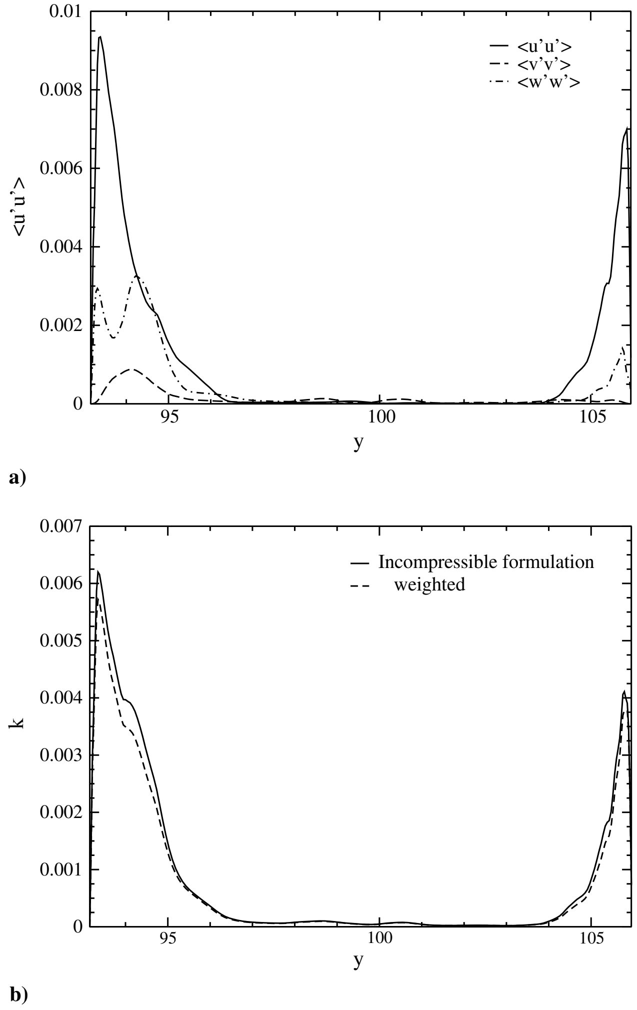

Fig. 14 Isolator exit turbulence levels, extracted from a single flowfield-averaged over z: a) rms velocity fluctuations and b) turbulence kinetic energy.

contraction ratio (the ratio of the area at the cowl lip to the exit area) is 2.345. Based on a Mach number of the stream that would enter the cowl under inviscid flow conditions ($M = 4.28$), the Kantrowitz limit is calculated to be 1.506. Thus, the present internal contraction ratio is well above the Kantrowitz limit recommended for the intake self-starting mode operation, requiring a moveable geometry or adjustable bleeds.

The root-mean-square velocity fluctuations across the isolator exit are shown in Fig. 14. The fluctuations are highest near the wall, with the streamwise component dominant. The relative size of the spanwise fluctuation is larger than in equilibrium boundary layers, suggesting that the boundary-layer flows on both sides of the isolator duct have not recovered from the strong distortions introduced by the geometry and the shock interactions. It is also significant that the fluctuations do not fall identically to zero in the core flow.

V. Conclusions

A large-eddy simulation of a hypersonic intake has been conducted. To simulate a realistic intake flowfield, the laminar flow was first computed and the boundary layer was tripped by triggering train of turbulent spots close to the intake leading edge. The turbulent spots grow with a lateral half-spreading angle of 3.4 deg along the first external compression ramp. The SWBLI interaction at the external compression corner was found to be insufficient to create flow separation. However, enhanced unsteady turbulent fluctuations were seen near the foot of the corner shock. Further downstream of the second external ramp (near the first convex corner), a strong impinging shock wave from the cowl leading edge was observed to create a small separated region, with high levels of turbulence fluctuations. The Korkegi correlation predicted the occurrence of separation quite well, but could not indicate whether this would result in a massive or contained separation. The presence of a discontinuity such as the convex corner had the capability to lock the separations and to keep them contained. This geometrical information is not embedded in the correlation. The avoidance of the coalescence of two shocks and the presence of the convex corner appears to control the flow separation by counteracting the adverse pressure gradient induced by shock impingement.

The perturbations from the vehicle-side turbulent boundary layer were found to enter the cowl-side boundary layer, which finally underwent transition at the end of the separation bubble caused by the cowl internal compression ramp. Large pressure fluctuations were observed near the turbulent reattachment of the cowl-corner separation bubble. The mean flow and turbulence structure at the isolator exit have been documented. This should enable more realistic simulations of fuel–air mixing and combustion processes.

The present study has clearly demonstrated the feasibility of LES of model-scale intakes. LES is easier when the walls are hot relative to the freestream, due to the increased natural viscosity of the flow. The present simulations were relatively modest in scale, with 9.6 million grid points and periodic spanwise boundary conditions for $Re = 4.6 \times 10^6$ based on intake length. Such simulations at small flight-test scale are also clearly feasible with present-day computers. Simulations with sidewalls or of axisymmetric intake designs will require more computer resources but are already feasible on massively parallel computers. Large-eddy simulation of a full-scale flight vehicle will remain out of reach for the near future. However, such cases may be relatively easier to compute with RANS methods, because the flows are less likely to suffer from laminar separations and transitional effects. It is necessary, however, to improve RANS modeling of shock-induced separation of turbulent boundary layers, and the LES data obtained from the present work as well as from simplified model problems are expected to be useful for this purpose.

Acknowledgments

This work was performed within the Long-Term Advanced Propulsion Concepts and Technologies (LAPCAT) project, supported by the European Union within the Sixth Framework Programme Priority 1.4, Aeronautic and Space, contract AST4-CT-2005-012282, coordinated by ESA's European Space Research and Technology Centre. We would like to acknowledge A. Mack and P. Gruhn for helpful discussions and S Karl for providing the DLR TAU code results.

References

[1] Billig, F. S., and Kothari, A. P., "Streamline Tracing: Technique for Designing Hypersonic Vehicles," *Journal of Propulsion and Power*, Vol. 16, No. 3, 2000, pp. 465–471. doi:10.2514/2.5591

[2] Dolling, D. S., "Fifty Years of Shock Wave/Boundary Layer Interaction Research: What Next?," *AIAA Journal*, Vol. 39, No. 8, 2001, p. 1517. doi:10.2514/2.1476

[3] Pagella, A., Babucke, A., and Rist, U., "Two-Dimensional Numerical Investigations of Small-Amplitude Disturbances in a Boundary Layer at $Ma = 4.8$: Compression Corner Versus Impinging Shock Wave," *Physics of Fluids*, Vol. 16, No. 7, 2004, pp. 2272–2281. doi:10.1063/1.1738414

[4] Dupont, P., Haddad, C., and Debieve, J. F., "Space and Time Organization in a Shock-Induced Separated Boundary Layer," *Journal of Fluid Mechanics* Vol. 559, 2006, pp. 255–277. doi:10.1017/S0022112006000267

[5] Steelant, J., "Achievement Obtained for Sustained Hypersonic Flight within the LAPCAT Project," 15th AIAA International Space Planes and Hypersonic Systems and Technologies Conference, Dayton, OH, AIAA Paper 2008-2578, 2008.

[6] Korkegi, R. H., "Comparison of Shock-Induced Two- and Three-Dimensional Incipient Turbulent Separation," *AIAA Journal*, Vol. 13, No. 4, 1975, pp. 534–535. doi:10.2514/3.49750

[7] Henckels, A., Gruhn, P., and Gülhan, A., "Design and Experimental Verification of a Scramjet Inlet in Frame of ESA's LAPCAT Program," *6th European Symposium on Aerothermodynamics for Space Vehicles* [CD-ROM], ESA, Paris, Nov. 2008.

[8] Pirozzoli, S., and Grasso, F., "Direct Numerical Simulation of Impinging Shock Wave/Turbulent Boundary Layer Interaction at $M = 2.25$," *Physics of Fluids*, Vol. 18, No. 6, 2006, pp. 1–17. doi:10.1063/1.2216989

[9] Loginov, M. S., Adams, N. A., and Zheltovodov, A. A., "Large-Eddy Simulation of Shock-Wave/Turbulent Boundary Layer Interaction," *Journal of Fluid Mechanics*, Vol. 565, 2006, pp. 133–169. doi:10.1017/S0022112006000930

[10] Wu, M., and Martin, M. P., "Direct Numerical Simulation of Supersonic Turbulent Boundary Layer over a Compression Ramp," *AIAA Journal*, Vol. 45, No. 4, 2007, pp. 879–889. doi:10.2514/1.27021

[11] Vreman, B., Geurts, B., and Kuerten, H., "A Priori Tests of Large Eddy Simulation of the Compressible Plane Mixing Layer," *Journal of Engineering Mathematics*, Vol. 29, No. 4, 1995, pp. 299–327. doi:10.1007/BF00042759

[12] Inagaki, M., Kondoh, T., and Nagano, Y., "A Mixed-Time-Scale SGS Model with Fixed Model-Parameters for Practical LES," *Journal of Fluids Engineering*, Vol. 127, No. 1, 2005, pp. 1–13. doi:10.1115/1.1852479

[13] Touber, E., and Sandham, N. D., "Oblique Shock Impinging on a Turbulent Boundary Layer: Low-Frequency Mechanisms," AIAA Paper 2008-4170, 2008.

[14] Yee, H. C., Sandham, N. D., and Djomeri, M. J., "Low-Dissipative High-Order Shock-Capturing Methods Using Characteristic-Based Filters," *Journal of Computational Physics*, Vol. 150, No. 1, 1999, pp. 199–238. doi:10.1006/jcph.1998.6177

[15] Sandham, N. D., Li, Q., and Yee, H. C., "Entropy Splitting for High-Order Numerical Simulation of Compressible Turbulence," *Journal of Computational Physics*, Vol. 178, No. 2, 2002, pp. 307–322. doi:10.1006/jcph.2002.7022

[16] Sandham, N. D., Lawal, A. A., and Yao, Y. F., "Large-Eddy Simulation of Transonic Turbulent Flow over a Bump," *International Journal of Heat and Fluid Flow*, Vol. 24, No. 4, 2003, pp. 584–595. doi:10.1016/S0142-727X(03)00052-3

[17] Krishnan, L., and Sandham, N. D., "Effect of Mach Number on the Structure of Turbulent Spots," *Journal of Fluid Mechanics*, Vol. 566, 2006, pp. 225–234. doi:10.1017/S0022112006002412

[18] Krishnan, L., and Sandham, N. D., "Strong Interaction of a Turbulent Spot with a Shock-Induced Separation Bubble," *Physics of Fluids*,

Vol. 19, No. 5, 2007, pp. 1–11.
doi:10.1063/1.2432158

[19] Yao, Y., Krishnan, L., Sandham, N. D., and Roberts G. T., “The Effect of Mach Number on Unstable Disturbances in Shock/Boundary-Layer Interactions,” *Physics of Fluids*, Vol. 19, No. 5, 2007, Paper 054104.
doi:10.1063/1.2720831

[20] Bogey, C., and Bailly, C., “A Family of Low Dispersive and Low Dissipative Explicit Schemes for Flow and Noise Computations,” *Journal of Computational Physics*, Vol. 194, No. 1, 2004, pp. 194–214.
doi:10.1016/j.jcp.2003.09.003

[21] Fisher, M. C., “Spreading of a Turbulent Disturbance,” *AIAA Journal*, Vol. 10, No. 7, 1972, pp. 957–959.
doi:10.2514/3.50265

[22] Singer, B. A., “Characteristics of a Young Turbulent Spot,” *Physics of Fluids*, Vol. 8, No. 2, 1996, pp. 509–521.

[23] Teramoto, S., “Large Eddy Simulation of Transitional Boundary Layer with Impinging Shock Wave,” *AIAA Journal*, Vol. 43, No. 11, 2005, pp. 2354–2363.
doi:10.2514/1.16140

[24] Lanson, F., and Stollery, J. L., “Some Hypersonic Intake Studies,” *The Aeronautical Journal*, Vol. 110, No. 1105, 2006, pp. 145–156.

[25] Stolz, S., “High-Pass Filtered Eddy-Viscosity Models for Large-Eddy Simulations of Compressible Wall-Bounded Flows,” *Journal of Fluids Engineering*, Vol. 127, 2005, pp. 666–673.
doi:10.1115/1.979652

[26] Garnier, E., and Sagaut, P., “Large Eddy Simulation of Shock/Boundary-Layer Interaction,” *AIAA Journal*, Vol. 40, No. 10, 2002, pp. 1935–1944.
doi:10.2514/2.1552

[27] Smart, M., “Scramjets,” *The Aeronautical Journal*, Vol. 111, No. 1124, 2007, pp. 605–619.

S. Fu
Associate Editor